ELSEVIER

Contents lists available at ScienceDirect

International Journal of Heat and Mass Transfer

journal homepage: www.elsevier.com/locate/ijhmt





Anisotropic Fourier Heat Conduction and phonon Boltzmann transport equation based simulation of time domain thermo-reflectance experiments

Siddharth Sauray, Sandip Mazumder

Department of Mechanical and Aerospace Engineering, The Ohio State University, Columbus, OH 43210, USA

ARTICLE INFO

Keywords: Thermo-reflectance TDTR phonon BTE Boltzmann Thermal conductivity Anisotropy

ABSTRACT

The anisotropic Fourier Heat Conduction Equation (FHCE) and the multidimensional phonon Boltzmann Transport Equation (BTE) were solved numerically in cylindrical coordinates and in time domain to simulate a Time Domain Thermo-Reflectance (TDTR) experimental silicon/aluminum substrate/transducer setup. The out-of-phase response of the probe laser was predicted at various beam offset distances for a pump laser pulse frequency of 80 MHz and modulation frequency of 10 MHz and compared against experimental measurements for a silicon substrate. The isotropic FHCE was also solved for comparison. Results show that the isotropic FHCE with bulk thermal conductivity of 145 W/m/K significantly underpredicts the out-of-phase temperature difference, particularly at smaller beam offsets. With an isotropic thermal conductivity of 105 W/m/K, the computed results match experimental data at smaller beam offsets well, but overpredicts the experimental data at larger beam offsets. An almost-perfect match is obtained by using an anisotropic thermal conductivity wherein the radial (inplane) thermal conductivity is set to 85 W/m/K and the axial (through-plane) conductivity is set to 130 W/m/K. The multidimensional frequency and polarization dependent phonon BTE is next solved. The BTE results for the out-of-phase temperature difference match experimental observations well at small and intermediate beam offsets, but overpredicts the experimental data at larger beam offsets. FHCE results are fitted to the BTE predictions, and the extracted (best fit) thermal conductivity is found to be 110 W/m/K.

1. Introduction

Time Domain Thermo-Reflectance (TDTR) is a noncontact optical pump probe technique that has found prolific usage for the study of thermal transport at small time and length scales. "Small" refers to length scales that are smaller or comparable to the mean free paths of the energy-carrying phonons in a semiconductor material. In a TDTR experiment, the sample is covered by a thin metallic layer called the transducer. It is heated using a modulated and pulsed laser beam resulting in surface temperature (reflectivity) oscillations. These oscillations are measured using a probe laser, which is also moved along the surface, i.e., away from the center of the pump laser, often referred to as beam offset, as illustrated in Fig. 1. The probe laser measures the transducer surface temperature at a fixed duration after the pump laser pulse, and this is referred to as the delay time. The phase lag between the pump and the probe laser is fitted to model results to extract the thermal conductivity. Consequently, a mathematical model that adequately describes the thermal transport in the system is required because,

fundamentally, the measurements are made at the surface, while thermal conductivity is a volumetric property.

The frequency-domain solution to the Fourier heat conduction equation (FHCE) is the most common and earliest mathematical model used for this purpose. First proposed by Cahill [1] for analyzing TDTR data, this approach has found prolific usage [2,3], and the Feldman algorithm [4] is used to treat multiple layers. Alternatively, numerical solution of the FHCE may be used to attain the same goal, as has been demonstrated by Saurav and Mazumder [5] for Frequency Domain Thermo-Reflectance (FDTR) experiments. Numerical solutions have the advantage that finite substrate thicknesses (as opposed to semi-infinite) and realistic boundary conditions, such as Newton cooling, can be easily incorporated into the model.

The vast majority of studies in which the thermal conductivity has been extracted from either TDTR or FDTR experiments have used the isotropic FHCE for fitting the measured phase lag, in which it has been assumed that the thermal conductivity is same in all directions, or isotropic. A notable study by Wilson and Cahill [6] showed that it is difficult to accurately fit the measured TDTR data with an isotropic

E-mail address: mazumder.2@osu.edu (S. Mazumder).

^{*} Corresponding author at: Department of Mechanical and Aerospace Engineering, The Ohio State University, Suite E410, Scott Laboratory, 201 West 19th Avenue, Columbus, OH 43210.

Nomenclature		r	radial coordinate or radius [m]
		r	position vector [m]
Α	area [m ²]	$\hat{\mathbf{s}}$	unit direction vector
c	specific heat capacity per unit volume [J m ⁻³ K ⁻¹]	t	time [s]
D	density of states per unit volume [m ⁻³]	T	absolute temperature [K]
f	number density function	и	internal energy [J m ⁻³]
f_0	equilibrium number density function	V	volume of cell [m ³]
$G_{\omega,p}$	spectral directionally integrated intensity $[Wm^{-2} rad^{-1}s]$	Z	axial coordinate or thickness [m]
G_C	contact conductance [W m ⁻² K ⁻¹]	0 1	
ħ	Dirac constant = $1.0546 \times 10^{-34} \text{ [m}^2\text{kg.s}^{-1}\text{]}$	Greek	3-
$I_{\omega,p}$	spectral directional phonon intensity [Wm ⁻² sr ⁻¹ rad ⁻¹ s]	ρ_T	density of transducer [kg m ⁻³]
$I_{0,\omega,p}$	equilibrium phonon intensity [Wm ⁻² sr ⁻¹ rad ⁻¹ s]	θ	polar angle [rad]
k_B	Boltzmann constant = $1.381 \times 10^{-23} \text{ [m}^2\text{kg.s}^{-2}\text{K}^{-1}\text{]}$	$oldsymbol{v}_{\omega,p}$	phonon group velocity vector [m s ⁻¹]
k_T	thermal conductivity of transducer [W m ⁻¹ K ⁻¹]	$ au_{\omega,p}$	spectral relaxation time scale [s]
ñ	unit surface normal vector	ω	angular frequency [rad s ⁻¹]
N_{band}	total number of spectral intervals (or bands)	ω_L	modulation frequency of pump laser [Hz]
N_{dir}	number of solid angles (or directions)	Ω	solid angle [sr]
p	phonon polarization index	ϕ	phase lag [rad]
q	heat flux vector [Wm ⁻²]	Ψ	azimuthal angle [rad]
ų Q			
Q	heat transfer rate [W]		

FHCE solution, particularly when the probe laser spot is significantly offset from the pump laser spot. They proposed a frequency-domain solution to the anisotropic FHCE, and demonstrated, at least for their particular experiment, that a superior fit can be obtained by using an anisotropic thermal conductivity in which the in-plane conductivity is significantly smaller than the through-plane conductivity.

The thermal conductivity extracted from both TDTR and FDTR experiments using the Fourier heat conduction equation has been found to change when the modulation frequency, laser spot size, and pulse widths of the pump laser are changed [1-3,7]. The Fourier law assumes that all energy carriers engage in infinite many collision (scattering) events regardless of the distance traversed. The dependence of thermal conductivity on the modulation frequency, laser spot size, or pulse width is attributed to the fact that when the laser modulation frequency is high, the thermal penetration depth, which is inversely proportional to the square root of the modulation frequency, is small, and can often be smaller than the mean free path of some of the energy-carrying phonons. Consequently, some phonons hardly scatter. This results in so-called ballistic-diffusive transport or quasi-ballistic transport. In this regime

of transport, the effective thermal conductivity has been found to be smaller than the bulk value—a phenomenon known as *thermal conductivity suppression* [7-9].

To capture the quasi-ballistic effects and predict the thermal conductivity suppression for different modulation frequencies, various enhancements to Fourier law-based models have been proposed. One class of these models make use of the Hyperbolic Heat Conduction Equation (HHCE) [10-12], which accounts for finite velocity of the phonons by introducing a relaxation time as a parameter [11]. However, in the HHCE, all phonons are assumed to have the same velocity regardless of their type and frequency. An extension of the HHCE is the two-parameter models [13], in which the diffuse and ballistic phonons are treated differently by introducing an additional term in the Fourier heat conduction equation that involves the characteristic ballistic heat transport length as an additional parameter. A two-band model has been proposed by Ramu and Bowers [14], in which a cut-off frequency was used to classify the phonons into ballistic and diffusive phonons. The ballistic phonons were then treated by introducing a higher-order correction term in the Fourier law that was derived from the phonon BTE. Wilson

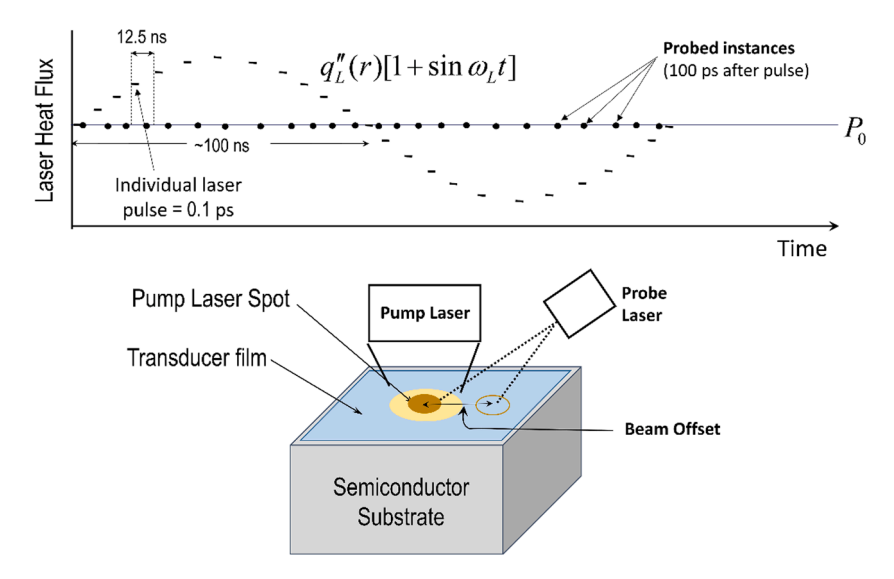


Fig. 1. Schematic representation of a TDTR experimental setup along with depiction of the modulated power pulse train. The numbers shown correspond to the conditions used for simulation in this study.

et al. [15] proposed a *two-channel model* specifically to account for nonequilibrium phonons in the context of TDTR experimental data interpretation for Al/Si/Ge alloys. In another class of models, referred to as *ballistic-diffusive models*, the phonon intensity was split into a diffusive component and a ballistic component. It was first proposed by Chen [16], and later expanded to complex three-dimensional geometry by Mittal and Mazumder [17,18]. More recently, a model that introduces a hydrodynamic term in the Fourier heat conduction equation—analogous to the advective term in the Navier-Stokes equation—has been proposed to capture ballistic effects [19].

The development of various approximate quasi-ballistic models that attempt to incorporate elements of the kinetic BTE into an otherwise diffusive Fourier model has been primarily prompted by the fact that the full-fledged phonon BTE is very challenging and time consuming to solve [20], although promising new algorithmic developments have been made on this front recently [21-26] to accelerate such computations. Peraud and Hadjiconstantinou [27] performed Monte Carlo simulations of phonon transport in a multidimensional optical pump-probe setup by using an energy-based deviational formulation. Only a single laser pulse was considered. This code was later used by Ding et al. [28] to simulate a single laser pulse of a TDTR experiment to demonstrate thermal conductivity suppression. Regner et al. [29] solved the one-dimensional (1D) BTE in frequency domain to extract the thermal conductivity accumulation and suppression functions. However, the influence of multidimensional thermal transport, which becomes apparent especially when the laser spot size is small, can only be captured by solving the multidimensional BTE. Ali and Mazumder [30] solved the full phonon BTE for TDTR experiments in a 2D planar setup and the model demonstrated thermal conductivity suppression and its dependence on the modulation frequency of the pump laser without the use of any additional tuning parameters. In recent studies, Saurav and Mazumder [31,32] simulated an FDTR experiment by solving the frequency and polarization dependent phonon BTE in cylindrical coordinates. The solution was advanced in time to a quasi-periodic state, enabling reliable extraction of the phase lag and exhibited good match with experimental measurements using two different relaxation time-scale models for acoustic phonons. These recent studies contrast previous studies [27,28] that only simulated a single laser pulse.

In TDTR simulations reported in the literature [27,28,30,33], the pump laser is modeled as a heat flux with a Gaussian profile. This is also the assumption used in analytical models. This is done to avoid complexities associated with modeling laser absorption (photon-phonon-electron interactions) in the transducer. These assumptions essentially reduce the computations to a problem in which a transient heat conduction problem is solved with a time-dependent heat flux on the top. Despite these simplifications, TDTR experiments are particularly challenging to simulate since the pump laser is pulsed and the pulse duration is extremely short. To the best of the authors' knowledge, there are only two previous studies that have reported simulation of a TDTR experimental setup using the multidimensional phonon BTE. A recent study by Hu et al. [33] conducted 3D simulations of a TDTR setup and demonstrated differences between BTE and FHCE predictions. The other study is a slightly earlier study by Ali and Mazumder [30]. The simulations performed by Ali and Mazumder [30] were in a 2D planar system and were not compared to experimental data. While this study was informative in understanding the numerical nuances of such a simulation, being 2D planar, it is not fully representative of the actual TDTR setup. Here, for the first time, an actual TDTR experimental setup is simulated by solving the phonon BTE in cylindrical coordinates. An isotropic phase-space is considered, and scattering is treated using the single-time relaxation approximation. The solution is advanced far enough in time such that the out-of-phase temperature change could be computed reliably and compared to experimental measurements. Additionally, both the isotropic and anisotropic FHCE equations are solved numerically to extract the thermal conductivity both by fitting the experimental data as well as by fitting the BTE results.

2. Theory

This section is divided into three subsections. In Section 2.1, the anisotropic FHCE is presented. In Section 2.2, the phonon BTE is presented, and Section 2.3 presents the connection between the BTE and overall energy conservation (First Law).

2.1. Anisotropic Fourier Heat Conduction Equation (FHCE)

In the absence of convection, radiation, and any heat source, the energy conservation equation (First Law) may be written as [34]

$$\frac{\partial u}{\partial t} = \rho c \frac{\partial T}{\partial t} = -\nabla \cdot \mathbf{q} \tag{1}$$

where u is the specific internal energy, t is time, and \mathbf{q} is the conductive heat flux. The volumetric specific heat capacity is denoted by c, while ρ and Tdenote the density and temperature of the medium, respectively. The heat flux, in general, may be expressed using the anisotropic Fourier law of heat conduction [34] as

$$\mathbf{q} = -\overline{\overline{k}} : \nabla T, \tag{2}$$

where \overline{k} denotes the thermal conductivity tensor. If the off-diagonal terms in the thermal conductivity tensor are neglected, then substituting Eq. (2) in Eq. (1), followed by expansion of the right-hand-side of the resulting equation in cylindrical coordinates, we obtain

$$\rho c \frac{\partial T}{\partial t} = k_r \frac{1}{r} \frac{\partial}{\partial r} \left(r \frac{\partial T}{\partial r} \right) + k_z \frac{\partial^2 T}{\partial z^2},\tag{3}$$

where k_r and k_z are the thermal conductivities in the radial (in-plane) and axial (through-plane) directions, respectively, as shown schematically in Fig. 2. In Eq. (3), any azimuthal variation has been neglected, implying that it is valid only for a two-dimensional (2D) axisymmetric system.

2.2. The phonon Boltzmann transport equation (BTE)

The BTE is suitable for modeling phonon transport in semiconductors, as phonons follow Bose-Einstein statistics and interact with each other via scattering events. The phonon BTE, under the single relaxation time approximation, may be written as [10,20]

$$\frac{\partial f}{\partial t} + \boldsymbol{v} \cdot \nabla f = \frac{f_0 - f}{\tau},\tag{4}$$

where f is the distribution function of an ensemble of phonons, f_0 is the equilibrium number density function, τ is the scattering time scale and υ is the phonon group velocity. In general, $f = f(t, \mathbf{r}, \mathbf{K})$, where \mathbf{r} denotes the position vector and \mathbf{K} denotes the wave-vector. Here, it is assumed that the wave-vector space (Brillouin zone) is isotropic. Hence, it can be expressed conveniently [10] using a unit direction vector, $\hat{\mathbf{s}}$, and a frequency ω . Thus, the distribution function, f, for each polarization f, is a function of seven independent variables, i.e., $f = f(t, \mathbf{r}, \hat{\mathbf{s}}, \omega, p)$, where the unit direction vector, $\hat{\mathbf{s}}$, may be expressed in terms of the azimuthal angle, ψ , and polar angle, θ , as [35]

$$\hat{\mathbf{s}} = \sin\theta \cos\psi \hat{\mathbf{i}} + \sin\theta \sin\psi \hat{\mathbf{j}} + \cos\theta \hat{\mathbf{k}}. \tag{5}$$

If the Cartesian coordinate system is used to describe space, for example, one may write the functional dependence of f as $f = f(t, x, y, z, \theta, \psi, \omega, p)$. In other words, for a three-dimensional (3D) geometry, f is a function of 8 independent variables. Since polarizations are discrete, it is customary to think of f as being a function of 7 independent variables, with the implicit understanding that it is different for different polarizations. The group velocity is also dependent on direction: $v = v(\widehat{s}, \omega, p)$. The equilibrium Bose-Einstein distribution, on the other hand, is

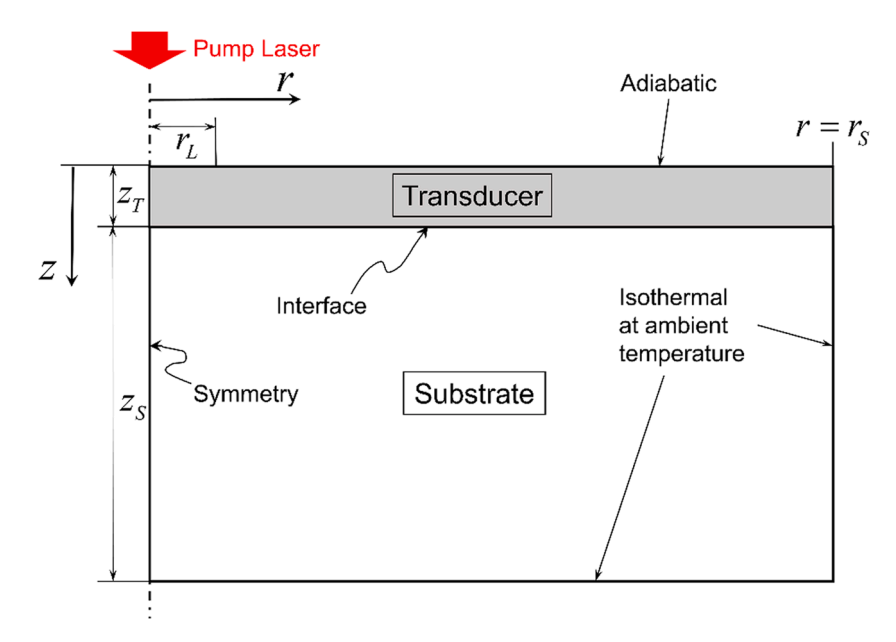


Fig. 2. Schematic of the two-dimensional axisymmetric model used in the current study, along with boundary conditions used.

direction independent: $f_0 = f_0(\omega, T)$, as is the relaxation time-scale: $\tau = \tau(\omega, T, p)$. Following the seminal work of Majumdar [33], a phonon intensity may be defined in terms of the distribution function:

$$\omega, p = I(t, \mathbf{r}, \hat{\mathbf{s}}, \omega, p) = |\mathbf{v}_{\omega, p}| \hbar \omega f D(\omega, p) / 4\pi
I_{0,\omega, p} = I_0(t, \mathbf{r}, \omega, p) = |\mathbf{v}_{\omega, p}| \hbar \omega f_0 D(\omega, p) / 4\pi,$$
(6)

where $D(\omega,p)$ is the density of states, and $I_{\omega,p}$ is the spectral directional phonon intensity, while $I_{0,\omega,p}$ is the equilibrium spectral phonon intensity. Substitution of Eq. (6) into Eq. (4) yields [36]

$$\frac{\partial I_{\omega,p}}{\partial t} + \boldsymbol{v}_{\omega,p} \cdot \nabla I_{\omega,p} = \frac{I_{0,\omega,p} - I_{\omega,p}}{\tau_{\omega,p}}.$$
 (7)

For any given frequency and polarization, the intensity, $I_{\omega p}$, is a function of time, 3 space variables (in 3D), and 2 directional variables, making Eq. (7) a six-dimensional equation. Furthermore, it needs to be solved for all frequency and polarizations in order to determine the heat flux, as is discussed in Section 2.3.

Solution of the BTE [Eq. (7)] necessitates boundary conditions for the intensity. Two types of boundary conditions are generally used [20]: (1) thermalizing, and (2) reflective. At a thermalizing boundary, phonons are emitted from it based on the equilibrium energy distribution and any phonon that strikes it immediately gets absorbed. The boundary condition is mathematically written as $I_{\omega,p}(t,\mathbf{r}_w,\widehat{\mathbf{s}}_o,\omega,p)=I_{0,\omega,p}(t,\mathbf{r}_w,\omega,p)$, where \mathbf{r}_w is the position vector of the boundary or wall, and $\widehat{\mathbf{s}}_o$ is the outgoing direction for the intensity.

2.3. Heat flux and energy conservation (First law)

Once the BTE [Eq. (7)] has been solved, the heat flux may be calculated from the phonon intensity using the relationship [20]

$$\mathbf{q}(t,\mathbf{r}) = \sum_{p} \int_{\omega_{\min,p}}^{\omega_{\max,p}} \int_{4\pi} I_{\omega,p}(t,\mathbf{r},\widehat{\mathbf{s}},\omega,p) \widehat{\mathbf{s}} d\Omega d\omega = \sum_{p} \int_{\omega_{\min,p}}^{\omega_{\max,p}} \mathbf{q}_{\omega,p}(t,\mathbf{r}) d\omega$$
(8)

where the integrals are over all solid angles Ω and the frequency range of each polarization; $\omega_{\max,p}$ and $\omega_{\min,p}$ are the maximum and minimum frequencies, respectively, corresponding to a given polarization, p. In Eq. (8), $\mathbf{q}_{\omega,p}$ denotes the spectral heat flux while \mathbf{q} denotes the total heat flux. Substitution of Eqs. (7) and (8) into Eq. (1), followed by some manipulation, yields [20]:

$$\frac{\partial}{\partial t} \left(\sum_{p} \int_{\omega_{\min,p}}^{\omega_{\max,p}} \frac{\hbar \omega D(\omega, p)}{\exp[\hbar \omega / k_{B} T] - 1} d\omega \right)$$

$$= -\sum_{p} \int_{\omega_{\min,p}}^{\omega_{\max,p}} \frac{1}{|\mathbf{v}_{\omega,p}|} \left[\frac{1}{\tau_{\omega,p}} \left(\frac{|\mathbf{v}_{\omega,p}| \hbar \omega D(\omega, p)}{\exp[\hbar \omega / k_{B} T] - 1} - G_{\omega,p} \right) - \frac{\partial G_{\omega,p}}{\partial t} \right] d\omega$$
(9)

where

$$G_{\omega,p} = \int_{4\pi} I_{\omega,p} d\Omega. \tag{10}$$

Eq. (9) is a nonlinear equation that may be solved to obtain the socalled pseudo-temperature [20,37], *T*, at any location within the computational domain and at any instant of time. In the section to follow, numerical techniques for solution of the anisotropic FHCE BTE are discussed.

3. Numerical procedure

3.1. Discretization of the anisotropic Fourier heat conduction equation (FHCE)

The anisotropic FHCE is discretized by applying the standard finite-volume procedure [38] to Eq. (3). The central difference scheme is used for spatial discretization, while the forward Euler (or explicit) method is used for discretization in time. Application of these procedures results in the following discrete equation for control volumes (or cells) within the substrate (interior cells in Fig. 3):

$$\rho c \Delta z_{k} \frac{2r_{j}\Delta r_{j}}{\Delta t} T_{j,k}^{n+1} = \rho c \Delta z_{k} \frac{2r_{j}\Delta r_{j}}{\Delta t} T_{j,k}^{n}
+ \left[\frac{k_{r}\Delta z_{k} (2r_{j} + \Delta r_{j})}{\Delta r_{j} + \Delta r_{j+1}} \right] \left(T_{j+1,k}^{n} - T_{j,k}^{n} \right) + \left[\frac{k_{r}\Delta z_{k} (2r_{j} - \Delta r_{j})}{\Delta r_{j} + \Delta r_{j-1}} \right] \left(T_{j-1,k}^{n} - T_{j,k}^{n} \right) ,
+ \left[\frac{4k_{z}r_{j}\Delta r_{j}}{\Delta z_{k} + \Delta z_{k+1}} \right] \left(T_{j,k+1}^{n} - T_{j,k}^{n} \right) + \left[\frac{4k_{z}r_{j}\Delta r_{j}}{\Delta z_{k} + \Delta z_{k-1}} \right] \left(T_{j,k-1}^{n} - T_{j,k}^{n} \right)$$
(11)

where the radius of the (j,k)-th cell's center is denoted by r_j , while the

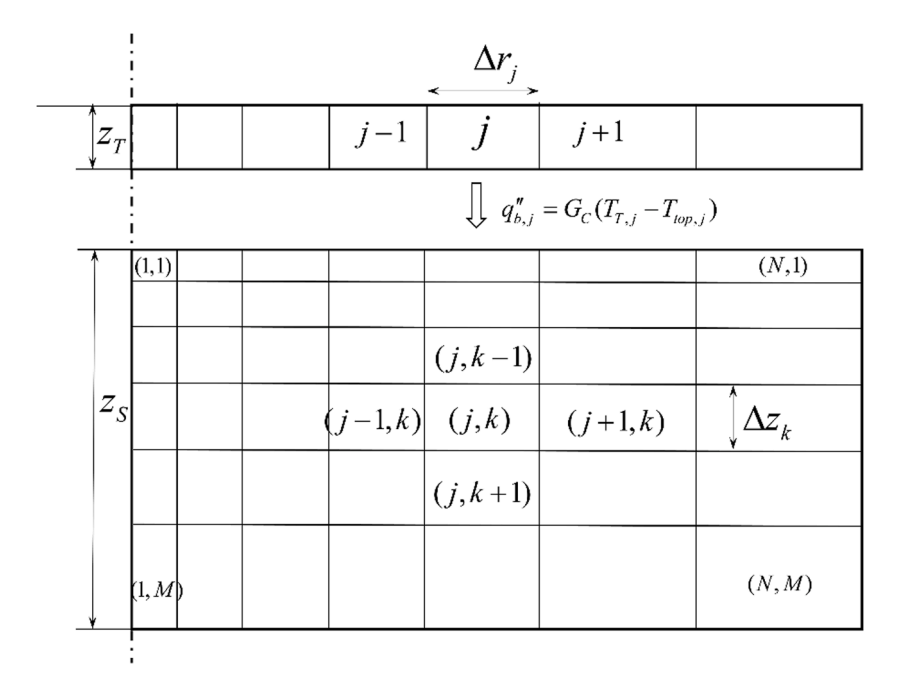


Fig. 3. Illustration of the mesh/stencil used for computations in the two different regions of the computational domain (transducer on top and substrate at the bottom).

radial span (grid size) is denoted by Δr_j . The axial span of the (j,k)-th cell is denoted by Δz_k . The superscripts n and n+1 denote values at the previous and current time-steps, respectively, such that $t=n\Delta t$, Δt being the time-step size. Likewise, finite-volume equations may be derived for cells adjacent to the boundaries. For example, for cells within the substrate and adjacent to the substrate-transducer interface, we obtain

$$\rho c \Delta z_{k} \frac{2r_{j} \Delta r_{j}}{\Delta t} T_{j,k}^{n+1} = \rho c \Delta z_{k} \frac{2r_{j} \Delta r_{j}}{\Delta t} T_{j,k}^{n}
+ 2q'_{b,j} |^{n} r_{j} \Delta r_{j} + \left[\frac{k_{r} \Delta z_{k} (2r_{j} - \Delta r_{j})}{\Delta r_{j} + \Delta r_{j-1}} \right] \left(T_{j-1,k}^{n} - T_{j,k}^{n} \right)
+ \left[\frac{4k_{z} r_{j} \Delta r_{j}}{\Delta z_{k} + \Delta z_{k+1}} \right] \left(T_{j,k+1}^{n} - T_{j,k}^{n} \right) + \left[\frac{4k_{z} r_{j} \Delta r_{j}}{\Delta z_{k} + \Delta z_{k-1}} \right] \left(T_{j,k-1}^{n} - T_{j,k}^{n} \right)$$
(12)

where q'_b is the heat flux from the transducer to the substrate (Fig. 3) and is discussed in more detail in Section 3.3.

3.2. The finite angle method (FAM)

The present work uses the finite angle method (FAM) [20,35] for solving the BTE [Eq. (7)]. The FAM is a variant of the Discrete Ordinates Method [35] that mitigates ray effects and guarantees energy conservation. In the FAM, the entire solid angle space is first split into a set of nonoverlapping smaller solid angles. These smaller solid angles may be based on equal subdivisions in θ and ψ , as shown in Fig. 4. The BTE [Eq. (7)] is first integrated over a volume [finite volume method in space on a structured mesh with cell index (j,k)], followed by finite solid angles to yield [20,35]:

$$\frac{\partial I_{l,\omega,p}}{\partial t}\Big|_{(j,k)}V_{(j,k)}\Omega_{i} + \left|\boldsymbol{\nu}_{\omega,p}\right|\sum_{f=1}^{N_{f,k}}I_{l,\omega,p,f(j,k)}(\mathbf{S}_{i}\cdot\widehat{\mathbf{n}}_{f})A_{f(j,k)}$$

$$= \frac{1}{\tau_{\omega,p,(j,k)}}(I_{o,\omega,p,(j,k)} - I_{l,\omega,p,(j,k)})V_{(j,k)}\Omega_{i}\forall i = 1, 2, ..., N_{dir}$$
(13)

where N_{dir} is the total number of discrete directions or finite solid angles, $V_{(j,k)}$ is the volume of the (j,k)-th cell, $A_{f(j,k)}$ is the area of the f-th face of the (j,k)-th cell, and

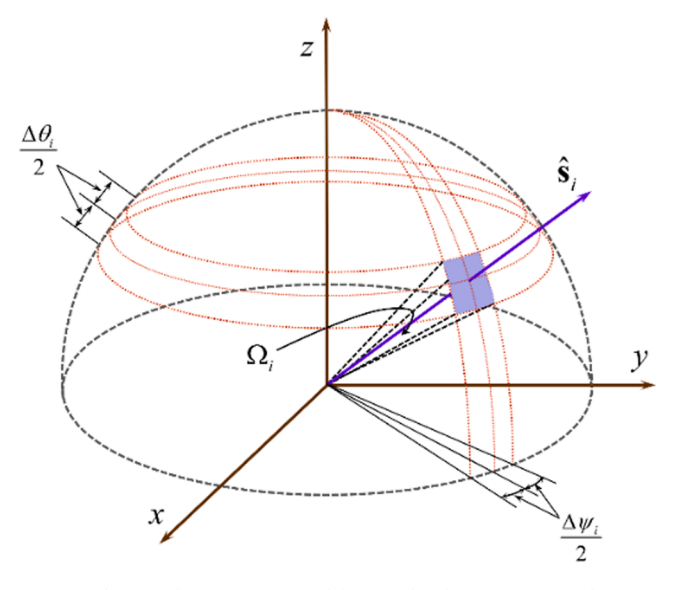


Fig. 4. Polar coordinate system used for angular discretization in the FAM.

$$\Omega_{i} = \int_{\Delta\Omega_{i}} d\Omega = \int_{\theta_{i} - \Delta\theta_{i}/2}^{\theta_{i} + \Delta\theta_{i}/2} \int_{\psi_{i} - \Delta\psi_{i}/2}^{\psi_{i} + \Delta\psi_{i}/2} \sin\theta d\theta d\psi = 2\sin\theta_{i}\sin\left(\frac{\Delta\psi_{i}}{2}\right) \Delta\psi_{i}, \tag{14}$$

and

$$\begin{aligned} \mathbf{S}_{i} &= \mathrm{cos}\psi_{i}\mathrm{sin}\left(\frac{\Delta\psi_{i}}{2}\right)\left[\Delta\theta_{i} - \mathrm{cos}(2\theta_{i})\mathrm{sin}(\Delta\theta_{i})\right]\widehat{\mathbf{i}} \\ &+ \mathrm{sin}\psi_{i}\mathrm{sin}\left(\frac{\Delta\psi_{i}}{2}\right)\left[\Delta\theta_{i} - \mathrm{cos}(2\theta_{i})\mathrm{sin}(\Delta\theta_{i})\right]\widehat{\mathbf{j}} \\ &+ \left(\frac{\Delta\psi_{i}}{2}\right)\mathrm{sin}(2\theta_{i})\mathrm{sin}(\Delta\theta_{i})\widehat{\mathbf{k}} \end{aligned} \tag{15}$$

The subscript i for the intensity now denotes an intensity along a line of sight passing through the center of the solid angle, i.e., in the direction $\hat{\mathbf{s}}_i$ (see Fig. 5). Finally, the face intensity in Eq. (13) is expressed in terms

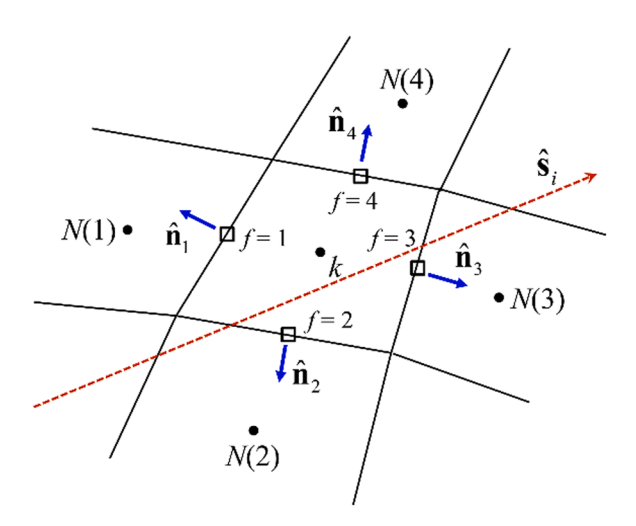


Fig. 5. Schematic representation of geometric quantities used for finite volume discretization of the BTE.

of cell-center intensities using the first-order upwind or step scheme [35]:

$$I_{i,\omega,p,f(j,k)} = \begin{cases} I_{i,\omega,p,j,k} & \text{if } \widehat{\mathbf{s}}_{i} \cdot \widehat{\mathbf{n}}_{f} > 0 \\ I_{i,\omega,p,N(f)} & \text{if } \widehat{\mathbf{s}}_{i} \cdot \widehat{\mathbf{n}}_{f} < 0 \end{cases}$$
(16)

where N(f) denotes the neighboring cell next to face f, as shown in Fig. 5. As a final note, in cylindrical coordinates, the volume appearing in

Eq. (13) may be determined using
$$V_{(j,k)} = \int\limits_{z_{b(j,k)}}^{z_{t(j,k)}} \int\limits_{r_{i(j,k)}}^{r_{o(j,k)}} 2\pi r dr dz$$
 where $r_{i(j,k)}$

and $r_{o(j,k)}$ are inner and outer radii, respectively, of the (j,k)-th cell, while $z_{b(j,k)}$ and $z_{t(j,k)}$ are bottom and top z-coordinates, respectively, of the same cell, as shown on Figs. 3 and 4. For any horizontal face, the area is given by $A_{f(j,k)} = \pi \left(r_{o(j,k)}^2 - r_{i(j,k)}^2 \right)$, while for any vertical face, the area is given by $A_{f(j,k)} = 2\pi r_f \left(z_{t(j,k)} - z_{b(j,k)} \right)$.

3.3. Treatment of the transducer

The transducer is a thin metallic layer placed on top of the substrate, as shown in Figs. 1 and 2. In this study, heat conduction in the transducer is treated using the isotropic FHCE. Furthermore, since the transducer is very thin, it is assumed that there is no temperature variation within the transducer in the z direction (Fig. 2). The only variation is in the r direction. Under this premise, the computational domain may be discretized using a structured mesh along the r direction, as shown in Fig. 3.

The governing equation for heat conduction in the transducer is a modified form of Eq. (3), and is written as

$$\rho_T c_T \frac{\partial T_T}{\partial t} = \frac{k_T}{r} \frac{\partial}{\partial r} \left(r \frac{\partial T_T}{\partial r} \right) + \frac{(\mathbf{q'}_t - \mathbf{q'}_b)}{z_T}$$
(17)

where ρ_T , c_T , k_T , and z_T are the density, specific heat capacity, thermal conductivity (assumed isotropic), and thickness of the transducer, respectively. The temperature of the transducer is denoted by T_T . The heat fluxes at the top and bottom surfaces of the transducer are denoted by q_t and q_b , respectively. The heat flux on the top surface is the energy supplied by the pump laser, and is a known quantity, written as

$$q'_{t} = \begin{cases} q'_{L}(r)[1 + \sin\omega_{L}t] & \text{for } t_{p} \leq t \leq t_{p} + \Delta t_{p} \\ 0 & \text{otherwise} \end{cases}$$
 (18)

where $q'_L(r)$ is the radially varying (assumed to be Gaussian) laser flux, and ω_L is the modulation frequency of the pump laser. The instances

where the laser pulses are turned on are denoted by t_p , while the pulse widths (durations) are denoted by Δt_p . The heat flux on the bottom surface of the transducer is not a known quantity. However, it can be related to the substrate through the relationship

$$q'_{b} = G_{C}(T_{T} - T_{top}) \tag{19}$$

where T_{top} is the local temperature on the top of the substrate surface, and G_C is the contact conductance between the transducer and the substrate. Although T_{top} is not directly known, it can be derived from the solution (of temperature) in the substrate, which in turn, requires solution of either the FHCE or the BTE in the substrate. This is done in a self-consistent manner, as described in Section 3.4.

As a final step, applying the finite-volume procedure [38] for discretization of Eq. (17), along with explicit (forward Euler) time discretization, we obtain

$$\rho_{T} c_{T} z_{T} \frac{2r_{j} \Delta r_{j}}{\Delta t} T_{T,j}^{n+1} = \rho_{T} c_{T} z_{T} \frac{2r_{j} \Delta r_{j}}{\Delta t} T_{T,j}^{n} + 2 \left(q_{t,j}^{"} \right|^{n} - q_{b,j}^{"} \right)^{n} r_{j} \Delta r_{j}
+ \left[\frac{k_{T} z_{T} (2r_{j} + \Delta r_{j})}{\Delta r_{j} + \Delta r_{j+1}} \right] \left(T_{T,j+1}^{n} - T_{T,j}^{n} \right) + \left[\frac{k_{T} z_{T} (2r_{j} - \Delta r_{j})}{\Delta r_{j} + \Delta r_{j-1}} \right] \left(T_{T,j-1}^{n} - T_{T,j}^{n} \right)$$
(20)

where superscripts n and n+1 denote values at the previous and current time-steps, respectively.

3.4. Solution algorithm

This section is split into two subsections. In the first subsection, the solution algorithm to determine the temperature distribution using the FHCE is described. In the second subsection, the solution algorithm to determine the temperature distribution using the phonon BTE is described.

3.4.1. Solution algorithm for the FHCE

In order to compute the temperature distribution and heat flux in a TDTR setup using the FHCE and the explicit (or forward Euler) time marching procedure, the following steps are executed:

- The temperature of the entire solution (computational) domain is first initialized. This includes the transducer and the substrate. This also includes nonisothermal boundaries, such as the transducer top, and the top surface of the substrate. Physically, the entire system is at the ambient temperature initially.
- 2. The flux at the bottom surface of the transducer is computed using Eq. (19).
- 3. The discretized form of the FHCE in the transducer [Eq. (20)] is marched forward explicitly by one time step to determine the temperature of the cells in the transducer.
- 4. The discretized form of the isotropic $(k_r = k_z)$ or anisotropic $(k_r \neq k_z)$ FHCE [Eqs. (11-12) and other similar equations for cells adjacent to boundaries] is marched forward explicitly by one time step to determine the temperature distribution $T_{j,k}$ inside the substrate.
- Eq. (19) is used again to compute the heat flux at the bottom surface of the transducer.
- 6. Steps 3–5 are repeated, i.e., the solution is marched forward in time. The temperature distributions obtained in Steps 3 and 4 serve as initial conditions for the next time step.

3.4.2. Solution algorithm for the BTE

Determination of the (pseudo-)temperature distribution and heat flux in a TDTR setup using the explicit (or forward Euler) time marching procedure requires the following steps:

- The temperature of the entire solution (computational) domain is first initialized. This includes nonisothermal boundaries, such as the transducer top. Physically, the entire system is at the ambient temperature initially.
- 2. The discretized form of the BTE [Eq. (13)] is marched forward explicitly by one time step to determine the spectral intensity, $I_{i,\omega,p}$. This intensity is then post-processed to compute the incident phonon intensity, $G_{\omega,p}$, using Eq. (10). Likewise, Eq. (8) may be used to compute the heat flux at locations of interest, e.g., at boundary surfaces.
- 3. The computed value of $G_{\omega,p}$ is then substituted into Eq. (9) and the resulting equation is solved using a nonlinear equation solver to determine the pseudo-temperature distribution at the next time step. This temperature distribution serves as the initial condition in the substrate for the next time step.
- The intensities obtained from the solution of the BTE can also be used to determine the heat flux at the top surface of the substrate using Eq. (8).
- 5. The heat flux at the top surface of the substrate is equal to the heat flux at the bottom surface of the transducer, q'_{bj} . Once this is known, Eq. (20) can be marched forward in time. Solution of Eq. (20) yields the transducer temperature.
- 6. With the heat flux and transducer temperature both being known, the temperature on the top of the substrate can now be computed using Eq. (19). This new temperature replaces the initial condition in Step 1 and represents the initial condition in the transducer for the next time step.
- 7. Steps 2–6 are repeated, i.e., the solution is marched forward in time.

4. Results and discussion

For the purposes of this study, the experimental setup and data reported by Wilson and Cahill [6] were used for reference and comparison. The substrate in this experiment is a silicon block and is covered by an aluminum transducer of thickness 80 nm. The modulation frequency of the pump, ω_L , is 9.8 MHz and the pump laser radius, r_{pump} , is 1.05 μ m. A Gaussian laser flux profile (in r) was used for all calculations. The duration of the heating pulse is 0.1 ps. The repetition or pulse rate of the laser is 80 MHz (every 12.5 ns) and the out-of-phase temperature response is measured at a delay time of 100 ps. The radius of the probe beam is the same as the pump beam. Since 80 MHz is not exactly divisible by 9.8 MHz, for convenience, 10 MHz was used for computations so that the time steps could be exactly aligned to both the laser modulation and the repetition rate.

Preliminary calculations were first conducted to estimate the thermal penetration depth (which indirectly affects the computational domain size), and the grid density necessary to adequately resolve the heat wave. Following this study, a computational domain with $z_s = 100$ μ m and r_S = 100 μ m was deemed adequate. For numerical calculations, a 100×100 nonuniform mesh with a stretching factor not exceeding 1.05 was used, as shown schematically in Fig. 3. The time marching scheme commenced with $\Delta t = 0.1$ ps (same as the laser pulse duration) and the time-step size was progressively increased to span the repetition rate of 12.5 ns using 1002 time-steps. The maximum time-step size used was 1.25 ps, which is dictated by the stability criterion of the explicit time marching (forward Euler) scheme used here for both the FHCE and the BTE. It is also small enough to resolve all scattering events in the BTE calculation. Isothermal boundary conditions (300 K) were applied to the side and bottom surfaces of the substrate, while an adiabatic boundary condition was applied to the top surface of the transducer beyond the laser spot (Fig. 2). In a previous study [5], Newton cooling boundary conditions, with heat transfer coefficients consistent with natural convection, were used for all boundary conditions, and it was found that the results did not change compared to the boundary conditions used here. The thermophysical properties of the aluminum transducer and bulk silicon are shown in Table 1. The nominal value of the interfacial

Table 1Thermophysical properties of the various materials used in the calculations.

	Silicon (bulk)	Aluminum
Density (kg/m ³)	2329	2689
Specific heat capacity (J/kg/K)	702	900
Thermal conductivity (W/m/K)	145	160

(between the substrate and the transducer) contact conductance, G_C , was taken to be 250 MW/m²/K, in keeping with Wilson and Cahill [6].

4.1. Extraction of thermal conductivity

In order to compare the computed results to experimental measurements and extract the thermal conductivity, the following procedure is adopted. First, time domain simulations of the TDTR setup are performed using the FHCE. From the computed temperature distributions, the temperature, Gaussian profile (in r) weighted area-averaged over the probe area on the surface of the transducer, is computed at all instances of time. Fig. 6 shows a plot of such a signal (solid black curve) over the final three cycles. On this plot, the temperature values corresponding to the delay times are marked, as shown by the red circles along with a zoomed image shown in the inset of Fig. 6. A sine curve is then fitted to the red circles, as shown by the dotted line. The frequency of this sine curve is the same as the modulation frequency ω_L [6]. The process is then repeated by offsetting the probe area from the center of the pulse laser, as shown in Fig. 1. The temperature at any offset radius, r_O , is then given by [6]

$$T(r_O) = T_{\infty} + A_{rO}\sin(\omega_L t + \phi_{rO}), \tag{21}$$

where $T(r_O)$ is the radially Gaussian profile weighted area-averaged probe temperature at location r_O , T_∞ is the ambient temperature, A_{rO} is the amplitude of the fitted sine curve at location r_O , and ϕ_{rO} is the phase lag from the sinusoidal pump laser signal with modulation frequency ω_L . The in-phase and out-of-phase components of the temperature at the location r_O are given by [6]

$$\Delta T_{in} = A_{rO}\cos(\phi_{rO}) \tag{22a}$$

$$\Delta T_{out} = A_{rO} \sin(\phi_{rO}) \tag{22b}$$

The two main inputs to the anisotropic FHCE are the radial and axial thermal conductivities. Since the computed temperatures change as a function of these two inputs, the in-phase and out-of-phase temperature responses can be changed by altering the radial and axial thermal conductivities. Wilson and Cahill [6] noted that the out-of-phase signal is particularly affected by the choice of k_r versus k_z , while the in-phase component is unaffected by that choice. Fig. 7 shows a plot of the out-of-phase temperature, ΔT_{out} , measured by Wilson and Cahill [6], as well as computed by our numerical model as a function of beam offset. Using the relaxation time scales reported by Ward and Briodo [43], we obtained a bulk thermal conductivity of 145 W/m/K. When the bulk value of $k_r = k_z = 145$ W/m/K is used, the out-of-phase response is severely underpredicted when compared to measured values. Since thermal conductivity is known to be suppressed at the nanoscale, $k_r =$ k_z = 105 W/m/K was attempted next. While this choice improved the results significantly, the ΔT_{out} was overpredicted for large beam offsets. This suggests that radial thermal transport is overpredicted when $k_r =$ $k_z = 105 \text{ W/m/K}$. Based on this premise, Wilson and Cahill [6] recommended lowering the k_r value relative to the k_z value. They obtained the best fit to the experimental data by using $k_z = 140 \text{ W/m/K}$ and $k_r = 80$ W/m/K.

In the present study, multiple combinations of k_r and k_z were used and the ΔT_{out} computed for various beam offset values. The least-square errors (L2Norm) between each predicted dataset and the experimentally measured dataset were then computed. The least-square errors were computed on the normalized error (difference between the pre-

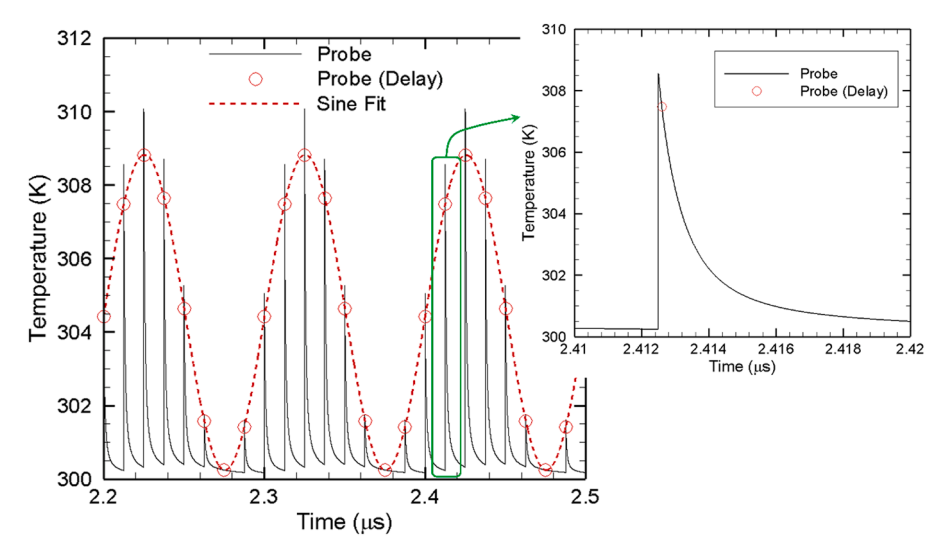


Fig. 6. Transducer temperature (averaged over probe area) computed using the anisotropic FHCE ($k_r = 85 \text{ W/m/K}$ and $k_z = 130 \text{ W/m/K}$) with no beam offset and a delay time of 100 ps.

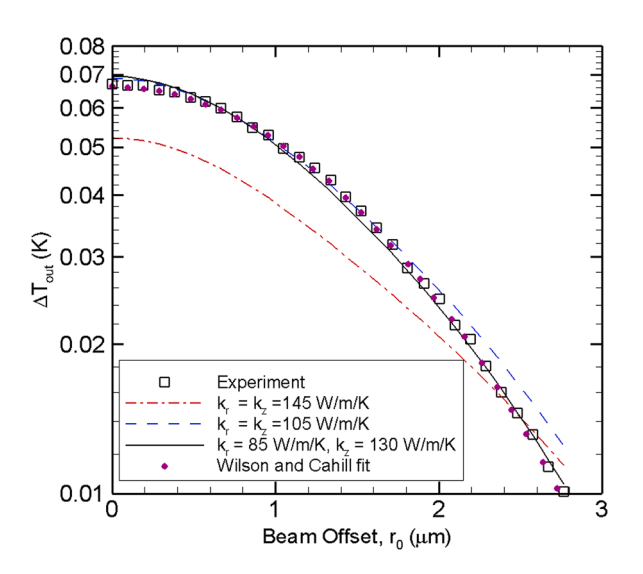


Fig. 7. Comparison of out-of-phase temperature response computed using the anisotropic FHCE and experimental data [6].

diction and experiment, normalized by the experimental value) rather than absolute errors. This is because for large beam offset values, the ΔT_{out} values are small, and using absolute error values, as opposed to normalized error values, would undermine their contributions. In our calculations, the best fit, based on minimization of the least-square normalized error, was obtained by using $k_z = 130 \text{ W/m/K}$ and $k_r = 85$ W/m/K, as shown in Fig. 7. The slight difference in the final fitted anisotropic thermal conductivity could be attributed to differences in the analytical model (the analytical model assumes semi-infinite media) used in [6] versus the numerical model used here, the fact that 10 MHz instead of 9.8 MHz was used as the pulse repetition rate, as well as the discretization errors in time and space in the numerical model. Also, the exact criteria used to obtain the fit may affect the results. Nonetheless, the results confirm the findings of Wilson and Cahill [6]; notably, that an anisotropic FHCE yields a better fit to measured TDTR data. In general, it was observed that predicted results for small beam-offset values are far more sensitive to changes in either k_r or k_z compared to those at large beam-offset values. In other words, it is easier to adjust k_r or k_z to obtain a better fit in the center of the plot shown in Fig. 7 than it is to obtain a fit at the ends.

4.2. BTE predictions

For BTE calculations, the frequency space was discretized, as shown in Fig. 8, with $N_{TA} = 14$, $N_{LA} = 24$, following previous studies [28, 39-41]. Likewise, following previous studies [40,41], the angular space was discretized using 4 azimuthal angles and 20 polar angles, resulting in a total of 80 finite solid angles or directions.

Scattering of phonons has been treated using a variety of approaches ranging all the way from scattering time scales derived from ab initio calculations with full treatment of the anisotropic Brillouin zone [42-44] to simplified parameterized single-time relaxation time-scale expressions. Here, the latter approach is used in keeping with the assumption of an isotropic wave-vector space (see Section 2.2) and also because these parameterized scattering time-scale expressions have been routinely used in engineering calculations [20-22,30-32,37,39,40,45]. For the scattering (or relaxation) time-scales of acoustic phonons, the following expressions proposed by Broido and co-workers [46] was used:

$$\tau_{N,p}^{-1} = A_p^N \omega^2 T [1 - \exp(-3T/\theta_D)]$$
 (23a)

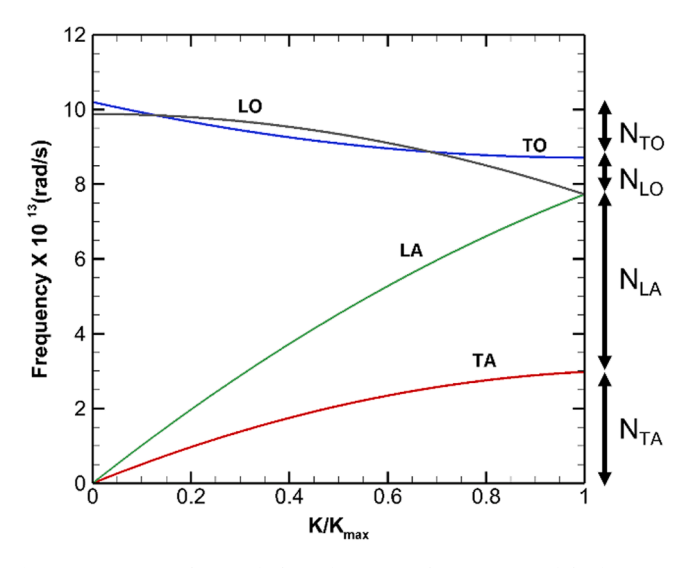


Fig. 8. Dispersion relation of silicon from [48]; discretization of the frequency space is also shown.

$$\tau_{U,D}^{-1} = A_D^U \omega^4 T [1 - \exp(-3T/\theta_D)]$$
 (23b)

where the subscripts N and U stand for Normal and Umklapp processes, respectively, and the subscript p stands for the polarization of the phonon, *i.e.*, either longitudinal acoustic (LA) or transverse acoustic (TA). The constants in Eq. (23) are as follows: $A_{LA}^N = 7.10 \times 10^{-20} \text{s.}$ rad $^{-2}\text{K}^{-1}$, $A_{TA}^N = 10.9 \times 10^{-20} \text{s.}$ rad $^{-2}\text{K}^{-1}$, $A_{LA}^U = 9.51 \times 10^{-47} \text{s}^3$. rad $^{-4}\text{K}^{-1}$, and $A_{TA}^U = 37.8 \times 10^{-47} \text{s}^3$.rad $^{-4}\text{K}^{-1}$. It is worth noting that although this model is parameterized (primarily, to allow convenient use), it was derived from first principles [46]. Optical phonons were also considered in this study. Although it is generally believed that optical phonons do not contribute significantly to thermal transport in silicon except at high temperature [39] because of their low group velocities, they do contribute significantly to storage of energy. Hence, they have the ability to affect the thermal diffusivity and, thereby, the phase lag. To highlight this point, for a crystalline material, the internal energy and the specific heat capacity at constant volume, which is the derivative of internal energy with respect to temperature, are given by [20]

$$u = \sum_{p} \int_{\omega_{\min p}}^{\omega_{\max p}} \frac{\hbar \omega D(\omega, p)}{\exp[\hbar \omega / k_B T] - 1} d\omega$$
 (24a)

$$c = \frac{du}{dT} = \frac{\hbar^2}{k_B T^2} \sum_{p} \int_{\omega_{\min p}}^{\omega_{\max p}} \frac{\omega^2 D(\omega, p) \exp[\hbar \omega / k_B T]}{(\exp[\hbar \omega / k_B T] - 1)^2} d\omega$$
 (24b)

Eq. (24b), when used in conjunction with the dispersion relations shown in Fig. 8 to compute the specific heat capacity of silicon at 300 K, yields a value of 625.4 J/kg/K, as opposed to the reported bulk value of 702 J/kg/K at 300 K. Limited data is available on the relaxation time scale for optical phonon scattering in silicon. In this study, the data published by Henry and Chen [47] were used. Fig. 9 shows the spectral mean free path data along with least-square curve-fits that were used to represent that scattered data in the present computations. The curve-fit expressions are as follows:

$$\Lambda_{LO} = A_{LO}\omega^2 + B_{LO}\omega + C_{LO} \tag{25a}$$

$$\Lambda_{TO} = A_{TO} \exp(-B_{TO}\omega) \tag{25b}$$

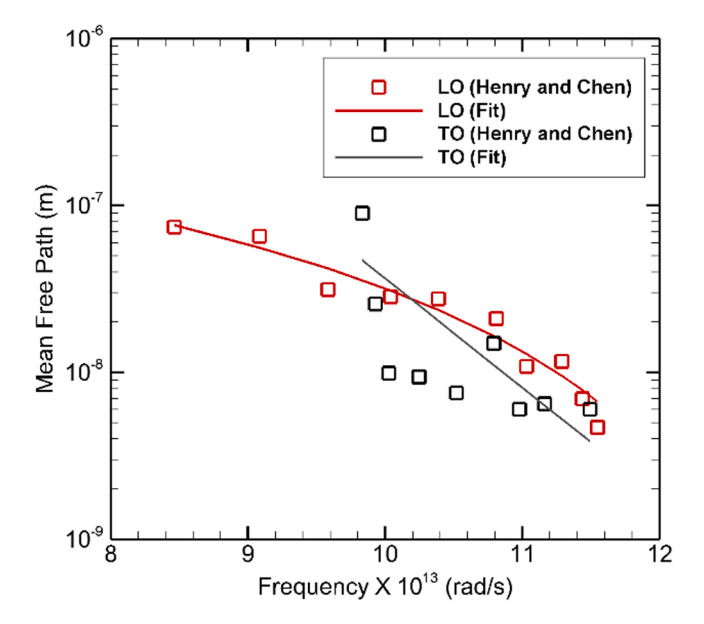


Fig. 9. Spectral mean free path of optical phonons, obtained from Henry and Chen [44], along with least-square curve-fits for the same data. LO = Longitudinal Optical; TO = Transverse Optical.

where Λ is the mean free path in meters, while ω is the frequency in rad/s. The constants in Eq. (22) are as follows: $A_{LO}=4.065\times 10^{-35}, B_{LO}=-1.039\times 10^{-20}, C_{LO}=6.641\times 10^{-7}, A_{TO}=0.1254,$ and $B_{TO}=1.51\times 10^{-13}$. The relaxation time-scale for optical phonon scattering were computed using $\tau=\Lambda/\upsilon$. The dispersion relationships for silicon, shown in Fig. 8, adopted from Pop [48], were used to compute the phonon group velocities, υ , for all frequencies and polarizations. As stated earlier, it is assumed that the wave-vector space is isotropic and, therefore, the dispersion relationship in only one lattice direction is necessary. Once the relaxation time-scales of the various phonons were computed, the Mathiessen rule [10] was used to compute the overall relaxation time-scale for scattering.

To bring to light the difficulty of BTE calculations for the problem at hand, a rough estimate is helpful. Since 40 bands and 80 angles are used, the calculation essentially entails time-marching 3200 partial differential equations on a mesh with 10,000 cells. For a modulation frequency of 10 MHz, the time-period for each cycle is 100 ns. Since approximately 8000 time-steps are used per cycle (1002 per pulse repetition) and the solution is advanced by roughly 10 cycles (determined by trial-and-error from the FHCE calculations) to attain quasi-periodic state, the simulations require approximately 80,000 time-steps. Using band-based parallelization over 40 processors (same as the number of bands), the calculations required approximately 184 h.

The out-of-phase temperature difference predicted by BTE calculations is shown in Fig. 10. It is evident that the predictions do not match experimental results at larger beam offset values. It appears that in the BTE results, radial transport of energy is stronger than suggested by the experimental data. This could be attributed to several factors: the assumption that the phonons are in equilibrium at the substratetransducer interface, the relaxation time scales from different sources used for the computations, the assumption of an isotropic Brillouin zone, and lack of detailed treatment of electron-phonon coupling at the interface. While electron-phonon coupling has been considered in previous work [49,50], it requires tuning of additional parameters. An attempt was also made to fit the BTE predictions using results of the FHCE with the goal of extracting an effective thermal conductivity, and this yielded a value (isotropic) of 110 W/m/K. The fit is shown in Fig. 10, as well. When thermal conductivity values of 105 and 115 W/m/K was tried, the ΔT_{out} predicted at larger beam off-set values (right end of figure) changed marginally, while the ΔT_{out} predicted at small beam offset values (left end of figure) changed significantly, resulting in

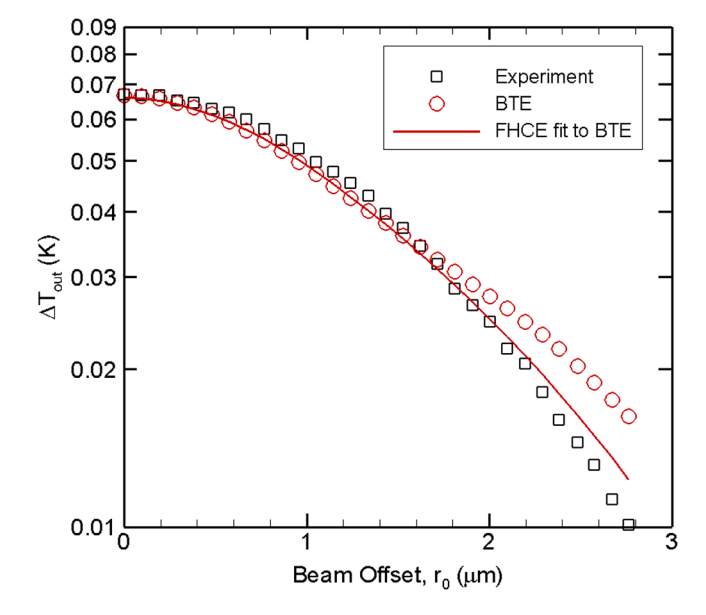


Fig. 10. Out-of-phase temperature response computed using the phonon BTE compared to experimental data [6]. FHCE fit to the BTE results is also shown.

a larger least-square error. In other words, the ΔT_{out} at large beam offset values is far less sensitive to the value of the thermal conductivity than for small beam offset values. It was found that the only way to better fit the BTE results would be to use an unrealistically large value of k_r (not shown). Since the FHCE and BTE are fundamentally different models, an exact fit should, perhaps, not be expected in the first place.

One of the key observations from our simulations is that the temporal decay of the temperature signal immediately after the pulse, as shown in the inset of Fig. 6, is extremely rapid and the shape of the decay curve sensitive to the model (FHCE versus BTE) that is used to replicate its behavior. Perhaps, in future TDTR experiments, if the out-of-phase temperature difference were recorded *simultaneously* at two different delay instances, such data would significantly aid in better understanding the shape of the delay curve and the subsequently extracted thermal conductivity. An interesting study would be to investigate how much the thermal conductivity changes if one or the other or both sets of data (from the two delay instances) are used. This may be a recommended direction of extension of currently used TDTR experimental setups.

5. Summary and conclusions

Time Domain Thermo-Reflectance (TDTR) is a routinely used stateof-the-art noncontact optical pump-probe technique for the study of thermal transport at sub-micron scales in semiconductor materials. In this study, two models are used to simulate a TDTR experimental setup in time domain and extract the thermal conductivity. One of these is the transient Fourier Heat Conduction Equation (FHCE); in particular, based on previous reports that anisotropy may be important to consider, the anisotropic FHCE is used. The second model is the full frequency and polarization dependent phonon Boltzmann Transport Equation (BTE). Both computations are conducted in a two-dimensional axisymmetric geometry in cylindrical coordinates. The thin metallic transducer film covering the substrate is modeled using the Fourier law and radial conduction in the transducer is included. Both computations are performed with a computational mesh comprised of 10,000 control volumes. For angular discretization of the BTE, 80 solid angles (directions) are used, while for discretization of the frequency space, 40 spectral intervals (or bands) are used. For time advancement, the explicit (forward Euler) procedure with unequal time step size starting at 0.1 ps and increasing up to 1.25 ps is used. The simulation is carried out until quasiperiodic state is reached. This requires approximately 10 modulation cycles (80 pulses) of the pump laser. For BTE calculations, the scattering time scales published by Ward and Briodo [43] were used to model acoustic phonon scattering in this study. Optical phonons were also included and the time-scales for scattering of optical phonons was estimated from Henry and Chen [44]. The BTE computations required approximately 184 h of wall clock time on a parallel computer system with 40 processors.

The out-of-phase response of the probe laser was predicted at various beam offset distances for a pump laser pulse frequency of 80 MHz and modulation frequency of 10 MHz and compared against experimental measurements [6] for a silicon substrate covered by an aluminum transducer. Predictions of the isotropic FHCE with a bulk isotropic ($k_r = k_z$) thermal conductivity of 145 W/m/K was found to severely underpredict the measured out-of-phase temperature difference ΔT_{out} . With the isotropic FHCE, the best fit to the experimental data was obtained with

 $k_r = k_z = 105$ W/m/K. It was found that an almost-exact match could be attained with

 k_z = 130 W/m/K and k_r = 85 W/m/K, confirming previous findings that suggested using an in-plane conductivity significantly smaller than the through-plane conductivity [6]. Results of solution of the BTE showed that the predicted ΔT_{out} values match experimental data quite well for small and intermediate beam offset values, but

 ΔT_{out} is severely underpredicted for large beam offset values. FHCE

results were fitted to the BTE results to extract an effective thermal conductivity, and an isotropic thermal conductivity $k_r=k_z=110~\rm W/$ m/K yielded the best fit. Attempts to fit the anisotropic FHCE to the BTE results failed as a close fit (better than the isotropic fit) could only be obtained with unrealistically large

 k_r values.

CRediT authorship contribution statement

Siddharth Saurav: Visualization, Validation, Methodology, Investigation, Formal analysis, Data curation. **Sandip Mazumder:** Writing – original draft, Supervision, Project administration, Funding acquisition, Formal analysis, Conceptualization.

Declaration of competing interest

The authors declare that they have no known competing financial interests or personal relationships that could have appeared to influence the work reported in this paper.

Data availability

Data will be made available on request.

Acknowledgments

This research was funded, in part, by Award number 2003747 by the National Science Foundation. The Ohio Supercomputer Center (OSC) and the Department of Mechanical and Aerospace Engineering at the Ohio State University are gratefully acknowledged for providing computational resources.

References

- D.G. Cahill, Analysis of heat flow in layered structures for time domain thermoreflectance, Rev. Sci. Instrum. 75 (2004) 5119.
- [2] K.T. Regner, D.P. Sellan, Z. Su, C.H. Amon, A.J.H. McGaughey, J.A. Malen, Broadband phonon mean free path contributions to thermal conductivity to thermal conductivity measured using frequency domain themroreflectance, Nat. Commun. 4 (2013) 1640.
- [3] A.J. Minnich, J.A. Johnson, A.J. Schmidt, K. Esfarjani, M.S. Dresselhaus, K. A. Nelson, G. Chen, Thermal conductivity spectroscopy technique to measure phonon mean free paths, Phys. Rev. Lett. 107 (2011) 095901.
- [4] A. Feldman, Algorithm for solutions of the thermal diffusion equation in a stratified medium with a modulated heating source, High Temperatures High Pressures 31 (1999) 293–298.
- [5] S. Saurav, S. Mazumder, On the determination of thermal conductivity from frequency domain Thermoreflectance experiments, J. Heat Transf. (ASME Transactions) 144 (2022) 013501.
- [6] R.B. Wilson, D.G. Cahill, Anisotropic failure of fourier theory in time-domain Thermoreflectance experiments, Nat. Commun. 5 (2014) 5075.
- [7] Y.K. Koh, D.G. Cahill, Frequency dependence of the thermal conductivity of semiconductor alloys, Phys. Rev. B 76 (2007) 075207.
- [8] A.J. Minnich, Determining phonon mean free paths from observations of quasiballistic thermal transport, Phys. Rev. Lett. 109 (2012) 205901.
- [9] C. Hua, A.J. Minnich, Transport regimes in Quasiballistic heat conduction, Phys. Rev. B 89 (2014) 094302.
- [10] C.L. Tien, A. Majumdar, F.M. Gerner, Microscale Energy Transport, Taylor and Francis, 1998.
- [11] P. Allu, S. Mazumder, Comparative assessment of deterministic approaches to modeling quasiballistic phonon heat conduction in multi-dimensional geometry, Int. J. Therm. Sci. 127 (2018) 181–193.
- [12] P. Allu, S. Mazumder, Hybrid Ballistic-Diffusive Solution to the Frequency-Dependent Phonon Boltzmann Transport Equation, Int. J. Heat Mass Transf. 100 (2016) 165–177.
- [13] Y. Ma, A two-parameter nondiffusive heat conduction model for data analysis in pump-probe experiments, J. Appl. Phys. 116 (2014) 243505.
- [14] A.T. Ramu, J.E. Bowers, A compact heat transfer model based on an enhanced Fourier law for analysis of frequency domain thermoreflectance experiments, Appl. Phys. Lett. 106 (2015) 263102.
- [15] R.B. Wilson, J.P. Fesser, G.T. Hohensee, D.G. Cahill, Two-channel model for nonequilibrium thermal transport in pump-probe experiments, Phys. Rev. B 88 (2013) 144305.

- [16] G. Chen, Ballistic-Diffusive Heat-Conduction Equations, Phys. Rev. Lett. 86 (11) (2001) 2297–2300.
- [17] A. Mittal, S. Mazumder, Generalized ballistic-diffusive formulation and hybrid S_n-P_n solution of the Boltzmann transport equation for phonons for non-equilibrium heat conduction, J. Heat. Transfer 133 (9) (2011). Article No. 092402.
- [18] A. Mittal, S. Mazumder, Hybrid Discrete Ordinates—Spherical Harmonics Solution to the Boltzmann Transport Equation for Phonons for Non-Equilibrium Heat Conduction, J. Comput. Phys. 230 (18) (2011) 6977–7001.
- [19] A. Beardo, M.G. Hennessy, L. Sendra, J. Camacho, T.G. Myers, J. Bafaluy, F. X. Alvarez, Phonon hydrodynamics in frequency-domain thermoreflectance experiments, Phys. Rev. B 101 (2020) 075303.
- [20] S. Mazumder, "Boltzmann transport equation based modeling of phonon heat conduction: progress and challenges,". Annual Review of Heat Transfer, Begell House Publications, 2021, pp. 71–130. 24, Chapter 3.
- [21] R. Li, E. Lee, T. Luo, Physics-informed neural networks for solving multiscale mode-resolved phonon Boltzmann transport equation, Mater. Phys. Today 19 (2021) 100429
- [22] J.Li Zhou, R, T. Luo, Physics-informed neural networks for solving time-dependent mode-resolved phonon Boltzmann transport equation, npj Comput. Mater. 9 (2022) 212.
- [23] Y. Hu, Y. Shen, H. Bao, Ultra-efficient and parameter-free computation of submicron thermal transport with phonon Boltzmann transport equation, Fund. Res. (2022), https://doi.org/10.1016/j.fmre.2022.06.007.
- [24] H.D. Tran, S. Saurav, P. Sadayappan, S. Mazumder, S. Sundar, Scalable parallelization for solution of phonon Boltzmann transport equation, in: ICS '23: Proceedings of the 37th International Conference on Supercomputing, 2023, pp. 215–226. Paper No. 175.
- [25] C. Zhang, Z. Guo, S. Chen, Unified implicit kinetic scheme for steady multiscale heat transfer based on the phonon Boltzmann transport equation, Phys. Rev. E 96 (2017) 063311.
- [26] C. Zhang, S. Chen, Z. Guo, L. Wu, A fast synthetic iterative scheme for the stationary phonon Boltzmann transport equation, Int. J. Heat Mass Transf. 174 (2021) 121308.
- [27] J-P.M. Peraud, N.G. Hadjiconstantinou, Efficient simulation of multidimensional phonon transport using energy-based variance-reduced Monte Carlo formulations, Phys. Rev. B 84 (2011) 205331.
- [28] D. Ding, X. Chen, A.J. Minnich, Radial Quasiballistic transport in time-domain thermo-reflectance studied using Monte Carlo simulations, Appl. Phys. Lett. 104 (2014) 143104.
- [29] K.T. Regner, A.J.H. McGaughey, J.A. Malen, Analytical interpretation of Nondiffusive phonon transport in thermoreflectance thermal conductivity measurements, Phys. Rev. B 90 (2014) 064302.
- [30] S.A. Ali, S. Mazumder, Phonon Boltzmann transport equation based modeling of time domain thermo-reflectance experiments, Int. J. Heat Mass Transf. 107 (2017) 607–621.
- [31] S Saurav, S. Mazumder, Phonon Boltzmann transport equation based modeling of frequency domain thermoreflectance experiments, in: Proceedings of the IMECE2022, Columbus, Ohio, 2022. October 30-November 3, Paper Number IMECE2022-95630.

- [32] S. Saurav, S. Mazumder, Extraction of thermal conductivity using phonon Boltzmann transport equation based simulation of frequency domain thermoreflectance experiments, Int. J. Heat Mass Transf. 204 (2023) 123871.
- [33] Y. Hu, R. Jia, J. Xu, Y. Sheng, M. Wen, J. Lin, Y. Shen, H. Bao, GiftBTE: an efficient deterministic solver for non-gray phonon Boltzmann transport equation, J. Phys. Condens. Matter 36 (2023) 025901.
- [34] H.S. Carslaw, J.C. Jaeger, Conduction of Heat in Solids, 2nd edition, Oxford University Press, London, 1959.
- [35] M.F. Modest, S. Mazumder, Radiative Heat Transfer, Fourth Edition, Academic Press, New York, 2021.
- [36] A. Majumdar, Microscale heat transfer in dielectric thin films, J. Heat Transf. 115 (1993) 7–16.
- [37] S. Mazumder, A. Majumdar, Monte Carlo study of phonon transport in solid thin films including dispersion and polarization, J. Heat Transf. 123 (2001) 749–759.
- [38] S. Mazumder, Numerical Methods for Partial Differential Equations: Finite Difference and Finite Volume Methods, 1st Edition, Academic Press, New York, 2016
- [39] A. Mittal, S. Mazumder, Monte Carlo study of phonon heat conduction in silicon thin films including contributions of optical phonons, J. Heat Transf. 132 (2010) 052402
- [40] S.A. Ali, G. Kollu, S. Mazumder, P. Sadayappan, A. Mittal, Large-scale parallel computation of the phonon Boltzmann transport equation, Int. J. Therm. Sci. 86 (2014) 341–351.
- [41] Y. Hu, Y. Shen, H. Bao, Optimized phonon band discretization scheme for efficiently solving the Nongray Boltzmann transport equation, J. Heat Transf. 144 (7) (2022) 072501.
- [42] K. Esfarjani, J. Garg, G. Chen, Modeling heat conduction from first principles, Annu. Rev. Heat Transfer 17 (2014) 9–47.
- [43] K. Esfarjani, G. Chen, Heat transport in silicon from first-principles calculations, Phys. Rev. B 84 (2011) 085204.
- [44] D.A. Broido, M. Malorny, G. Birner, N. Mingo, Intrinsic lattice thermal conductivity of semiconductors from first principles, Appl. Phys. Lett. 91 (2007) 231922.
- [45] J.Y. Murthy, S.V.J. Narumanchi, J.A. Pascual-Gutierrez, T. Wang, C. Ni, S. R. Mathur, Review of Multiscale simulation in submicron heat transfer, Int. J. Multiscale Comput. Eng. 3 (2005) 5–32.
- [46] A. Ward, D.A. Broido, Intrinsic phonon relaxation times from first principles studies of the thermal conductivities of Si and Ge, Phys. Rev. B 81 (8) (2010) 085205
- [47] A.S. Henry, G. Chen, Spectral phonon transport properties of silicon based on molecular dynamics simulations and lattice dynamics, J. Comput. Theor. Nanosci. 5 (2) (2008) 141–152.
- [48] E. Pop, Self-heating and scaling of thin body transistors. PhD. Dissertation, Department of Electrical Engineering, Stanford University, 2004.
- [49] K.T. Regner, L.C. Wei, J.A. Malen, Interpretation of thermoreflectance measurements with a two-temperature model including non-surface heat deposition, J. Appl. Phys. 118 (2015) 235101.
- [50] C. Hua, X. Chen, N.K. Ravichandran, A.J. Minnich, Experimental metrology to obtain thermal phonon transmission coefficients at solid interfaces, Phys. Rev. B 95 (2017) 205423.